Superconductor Science and Technology

PAPER

Determining the absolute value of magnetic penetration depth in small-sized superconducting films

IOP Publishing | Superconductor Science and Technology
Supercond. Sci. Technol. **34** (2021) 085022 (8pp) https://doi.org/10.1088/1361-6668/ac10fb

Determining the absolute value of magnetic penetration depth in small-sized superconducting films

Ruozhou Zhang[1,2,6], **Mingyang Qin**[1,2,6], **Lu Zhang**[3], **Lixing You**[3], **Chao Dong**[4], **Peng Sha**[4], **Qihong Chen**[1], **Jie Yuan**[1,5] and **Kui Jin**[1,2,5,*]

[1] Beijing National Laboratory for Condensed Matter Physics, Institute of Physics, Chinese Academy of Sciences, Beijing 100190, People's Republic of China
[2] School of Physical Sciences, University of Chinese Academy of Sciences, Beijing 100049, People's Republic of China
[3] Shanghai Institute of Microsystem and Information Technology, Chinese Academy of Sciences, Shanghai 200050, People's Republic of China
[4] Institute of High Energy Physics, Chinese Academy of Sciences, Beijing 100049, People's Republic of China
[5] Songshan Lake Materials Laboratory, Dongguan, Guangdong 523808, People's Republic of China

E-mail: kuijin@iphy.ac.cn

Received 14 April 2021, revised 21 June 2021
Accepted for publication 2 July 2021
Published 15 July 2021

Abstract

In the previous four decades, the two-coil mutual inductance (MI) technique has been widely employed in characterizing magnetic penetration depth, λ, of superconducting films. However, the conventional methods used to obtain λ are not applicable to small-sized films with common shapes, which limits the application of the MI technique in superconductivity research. Here, we first employed the fast wavelet collocation (FWC) method to a two-coil system and then proposed the possibility of directly obtaining the absolute λ of polygonal superconducting films with arbitrary sizes. To verify its accuracy and advantages, we extracted the λ values of square NbN films with different sizes using the FWC and conventional flux leakage subtraction (FLS) methods. Notably, the FLS method fails for a $5 \times 5\,\mathrm{mm}^2$ film, which is attributed to the significant current peak at the film edge. In contrast, the absolute λ extracted using the FWC method was independent of the film size. Finally, we established the applicability of the FWC method to large coil spacings, which may pave the way for integrating high-accuracy λ measurements with the ionic liquid gating technique.

Keywords: magnetic penetration depth, two-coil mutual inductance technique, superconducting film, fast wavelet collocation method

(Some figures may appear in colour only in the online journal)

1. Introduction

As a key physical parameter for superconductors, the magnetic penetration depth, λ, links macroscopic electrodynamics with the microscopic mechanism of superconductivity [1]. First, λ^{-2} is proportional to the superfluid density, n_s, and its temperature dependence, $\lambda^{-2}(T)$, encodes the information on paring symmetry and multiband superconductivity [2–4]. Second, by further extrapolating to the zero-temperature limit, the superfluid phase stiffness, $\rho_{s0} \propto \lambda^{-2}(T \to 0)$, could be extracted, which represents the resiliency of the superconducting phase under quantum or thermal fluctuations [5–9]. Third, according to the London phenomenological model, λ^2 is proportional to the effective mass, m^*, which could directly reflect

[6] These authors contributed equally to this work.
[*] Author to whom any correspondence should be addressed.

the impact of a quantum critical point [10–12]. In addition, the performances of most applicable superconducting devices depend on λ, e.g. the surface resistance, R_s, of microwave filters [13] and the superheating field, B_{sh}, of radio-frequency cavities in accelerators [14, 15]. That is, high-precision measurement of the absolute value of λ is crucial for elucidating the mechanism of superconductivity and exploring the applications of superconductors.

However, measuring the absolute value of λ accurately is difficult because λ is on the order of thousands of angstroms. Currently, scientists have developed various techniques [16, 17], among which the two-coil mutual inductance (MI) technique is of particular interest. Owing to its simplicity, no destruction, and high sensitivity, the technique has been used to characterize λ in a wide range of superconducting films. Over the previous 40 years, the MI technique has provided insight into the nature of superconductivity, including the Berezinskii-Kosterlitz-Thouless transition in Al and NbN thin films [18, 19], quantum criticality in strongly underdoped $Y_{1-x}Ca_xBa_2Cu_3O_{7-\delta}$ ultrathin films [7], and the scaling law between ρ_{s0} and critical transition temperature, T_c, in $La_{2-x}Sr_xCuO_4$ films [20]. Recently, Jia *et al* [21] reported a dome-shaped superconducting region in K-absorbed FeSe films using an *in situ* MI device in a multifunctional scanning tunneling microscope, demonstrating the advantage of the MI technique in characterizing fragile samples.

In general, a MI device consists of a drive coil and a pickup coil, which are coaxially located on the same side (*reflection*-type) or opposite sides (*transmission*-type) of the superconducting film. When the film enters the Meissner state, the magnetic field produced by the alternating current in the drive coil is expelled by the induced screening current in the film. Consequently, the pickup coil voltage, V, or equivalent MI, M, undergoes an instantaneous change, from which the absolute value of λ can be extracted [22–25].

For the *reflection*-type MI setup, it is easy to implement further manipulations on the film [26–28] because both coils are under the substrate and the top side of the film is free. However, it is difficult to achieve high-precision measurement of λ when using this configuration. This is because there is no method for eliminating the errors arising from the uncertainties in the coil geometry, most of which are owing to the nonideal aspects of coil windings and thermal shrinkage when the sample is cooled down. In contrast, for the *transmission*-type MI setup, these uncertainties can be removed by normalizing the measured MI, M_{exp}, to its normal state value, $M_{exp}(T > T_c)$ [24, 25]. Moreover, when the radius of the film is infinite, the normalized MI, $M_{exp}/M_{exp}(T > T_c)$, can be expressed analytically; the expression was first derived by Clem *et al* [29]. In practice, the finite size of the film allows some magnetic flux leaks around the film edge, thus resulting in residual coupling, M_1. Notably, it was established that M_1 is independent of λ and depends only on the shape of the film [24, 30]; thus it can be evaluated experimentally by substituting a thick Nb film with the same shape as the sample. Thereafter, λ can be extracted from the corrected MI $(M_{exp} - M_1)/M_{exp}(T > T_c)$. This method has been widely used, and it is referred to as the flux leakage subtraction (FLS) method in this study.

However, the FLS method preserves high precision only for small $M_1/M_{exp}(T > T_c)$ [24, 25], which intuitively requires a large film size. Therefore, Fuchs *et al* [31] suggested a film with a diameter greater than 50 mm for accuracy. However, the preparation of high-quality large-sized superconducting films is challenging. Although the conventional numerical model is independent of the film size, it can only deal with circular films [25]. For small-sized films with common shapes such as squares, an accurate method for extracting the absolute λ from M is required.

In this study, we first employed the fast wavelet collocation (FWC) method to extract the absolute λ from the MI data, which in principle applies to polygonal superconducting films with arbitrary sizes. Additionally, the details of the numerical model are presented. To evaluate the accuracy and advantages, we compared the values of λ obtained using the FWC method with those obtained using the FLS method.

2. Experimental methods

The inset of figure 1 shows a schematic of our *transmission*-type MI device, in which the drive and pickup coils are coaxially located on opposite sides of the film. Both coils were wound using 40 μm oxygen-free copper wires with insulation coating. Their inner diameter was 0.5 mm, the outer diameter was 1.3 mm, and the length was 1.6 mm. The separation between the two coils was approximately 1 mm. The device was thermally connected to a 3 K platform of a Montana Instruments cryocooler. The drive current had a frequency of 10 kHz and an amplitude of 2 mA, supplied by a Stanford Research SR830 lock-in amplifier. It is estimated that the excitation field at the film center is ~93 μT.The induced voltage, $V = V_x + iV_y$, in the pickup coil was measured using the same lock-in amplifier with a reference phase of 90°. More details can be found in our previous work [32].

The MI M of the two coils can be determined as

$$M = \frac{V_x}{\omega I_d} + i\frac{V_y}{\omega I_d}, \quad (1)$$

where ω is the angular frequency and I_d is the amplitude of the drive current. The first term in equation (1) represents inductive coupling, whereas the second represents resistive coupling. Except at temperatures near T_c, the film response is purely inductive and the resistive coupling is negligible [25].

We fabricated high-quality NbN films via reactive DC magnetron sputtering, as detailed in [33]. Films with sizes of $10 \times 10\,mm^2$ (NbN#1) and $5 \times 5\,mm^2$ (NbN#2) were grown in the same branch. The substrates were (100)-oriented MgO single crystals. The thickness of the films was 6.5 ± 0.2 nm, as characterized by x-ray reflectivity.

3. Numerical model

The role of our numerical model is to establish a one-to-one correspondence between λ and M. In principle, two types of

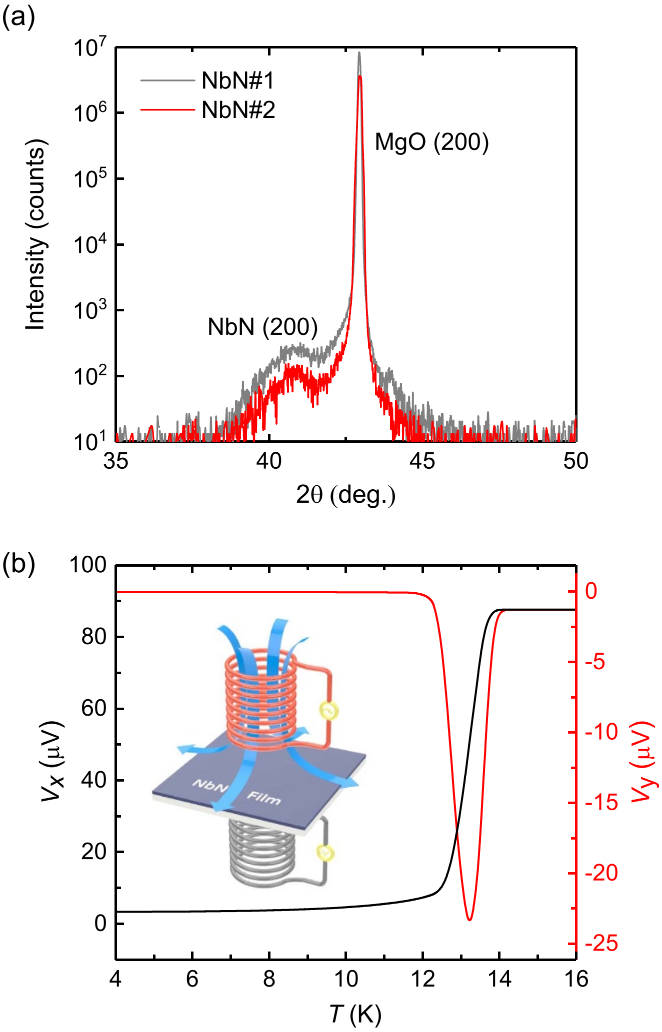

Figure 1. (a) x-ray diffraction patterns of NbN#1 and NbN#2. (b)Temperature dependence of the pickup coil voltage for NbN#1. The black and red curves represent the real and imaginary components of the pickup coil voltage, respectively. The inset shows the schematic illustration of the MI device.

currents contribute to MI M. One is the alternating current in the drive coil. The other is the screening current in the superconducting film, which needs to be carefully determined.

We consider a polygonal superconducting film placed on the xy plane. The thickness of the film is d, and the projection of the film on the xy plane is a polygon Ω. We assume that the vector potential, $\mathbf{A_d} = A_{dx}\widehat{\mathbf{x}} + A_{dy}\widehat{\mathbf{y}}$, generated by the drive current and screening current density $\mathbf{j_s} = j_{sx}\widehat{\mathbf{x}} + j_{sy}\widehat{\mathbf{y}}$ in the film are parallel to the film surface. Thereafter, employing Londons and Maxwells equations, $j_{s\alpha}\,(\alpha = x, y)$ is given by [24, 25]

$$j_{s\alpha}(\mathbf{r}) + \frac{d_{\mathrm{eff}}}{4\pi\lambda^2}\int_{\Omega} \mathrm{d}^2\mathbf{r}'\frac{j_{s\alpha}(\mathbf{r}')}{|\mathbf{r}-\mathbf{r}'|} = -\frac{1}{\mu_0\lambda^2}A_{d\alpha}(\mathbf{r}), \quad (2)$$

where $\mathbf{r} = x\widehat{\mathbf{x}} + y\widehat{\mathbf{y}}$ is the coordinate in Ω, $d_{\mathrm{eff}} = \lambda\sinh(d/\lambda)$ is the effective thickness and $\mu_0 = 4\pi\times10^{-7}\mathrm{N\,A^{-2}}$ is the vacuum permeability.

Equation (2) is a two-dimensional Fredholm integral equation of the second kind with a weakly singular kernel. This type of equations are of great importance in various engineering application fields [34], while their solution is an unresolved problem until the 21st century. We propose to solve equation (2) by the FWC algorithm, which was first developed by Chen *et al* [34]. Its significant computational efficiency and attractive convergence properties have been demonstrated in [34–36]. In the rest of this section, we will take the rectangular film as an example to describe the calculation steps of the FWC method.

First, we subdivide the polygon Ω into several triangles, and there is at most one common edge or vertex for two different triangles. A rectangular film with a length of $2a$ and a width of $2b$ can be divided into two triangles: $\Delta_0 = \left\{(x,y)\in\mathbb{R}^2 : x \geqslant -a, y \leqslant b, ay - bx \geqslant 0\right\}$ and $\Delta_1 = \{(x,y)\in\mathbb{R}^2 : x \leqslant a, y \geqslant -b, ay - bx < 0\}$. Because Δ_0 and Δ_1 can be affinely mapped onto the unit triangle $E = \left\{(x,y)\in\mathbb{R}^2 : 0 \leqslant x \leqslant y \leqslant 1\right\}$, equation (2) can be rewritten as

$$\begin{aligned}
&\widetilde{j_{s\alpha}}^{1}(x,y) + \frac{d_{\mathrm{eff}}}{2\pi\lambda^2}\left[b\left(K\widetilde{j_{s\alpha}}^{1}\right)\left(x,y,\frac{b}{a}\right) + a\left(K\widetilde{j_{s\alpha}}^{2}\right)\left(y,x,\frac{a}{b}\right)\right] \\
&\qquad = f_\alpha(x,y), \\
&\widetilde{j_{s\alpha}}^{2}(x,y) + \frac{d_{\mathrm{eff}}}{2\pi\lambda^2}\left[b\left(K\widetilde{j_{s\alpha}}^{1}\right)\left(y,x,\frac{b}{a}\right) + a\left(K\widetilde{j_{s\alpha}}^{2}\right)\left(x,y,\frac{a}{b}\right)\right] \\
&\qquad = f_\alpha(y,x),
\end{aligned} \quad (3)$$

where $\widetilde{j_{s\alpha}}^{1}(x,y) = j_{s\alpha}(2ax - a, 2by - b)$, $\widetilde{j_{s\alpha}}^{2}(x,y) = j_{s\alpha}(2ay - a, 2bx - b)$, $f_\alpha(x,y) = -\frac{1}{\mu_0\lambda^2}A_{d\alpha}(2ax - a,\ 2by - b)$, and the effect of operator K is $(KF)(x,y,t) = \int_E \mathrm{d}x'\mathrm{d}y'\frac{F(x',y')}{\sqrt{(x'-x)^2 + t^2(y'-y)^2}}$.

Next, we expand $\widetilde{j_{s\alpha}}^{\beta}$ $(\alpha = x, y, \beta = 1, 2)$ using multiscale wavelets $\{\omega_{ij}\}$ (see appendix A1a) as

$$\widetilde{j_{s\alpha}}^{\beta}(x,y) = \sum_{i=0}^{n}\sum_{j=0}^{\omega(i)} u_{ij\alpha}^{\beta}\omega_{ij}(x,y), \quad (4)$$

where i and j are integers, $\omega(0) = 3$, $\omega(i) = 9\times4^{i-1}\,(i \geqslant 1)$ and $n \geqslant 1$ is the highest level of ω_{ij} (for rectangular films, we take $n = 6$ [35]). Thereafter, by substituting equation (4) into equation (3) and applying collocation functional $\ell_{i'j'}$ (see appendix A2a) on both sides of equation (3), we obtain the matrix equation

$$\sum_{i=0}^{n}\sum_{j=0}^{\omega(i)}\left[\begin{pmatrix} E_{i'j'ij} & 0 \\ 0 & E_{i'j'ij}\end{pmatrix} + \frac{d_{\mathrm{eff}}}{2\pi\lambda^2}\begin{pmatrix} bK_{i'j'ij}^{11} & bK_{i'j'ij}^{12} \\ bK_{i'j'ij}^{21} & bK_{i'j'ij}^{22}\end{pmatrix}\right]\begin{pmatrix} u_{ij\alpha}^{1} \\ u_{ij\alpha}^{2}\end{pmatrix} = \begin{pmatrix} F_{i'j'\alpha}^{1} \\ F_{i'j'\alpha}^{2}\end{pmatrix}. \quad (5)$$

The elements of coefficient matrix can be calculated as follows:

$$\begin{aligned}
E_{i'j'ij} &= \langle \ell_{i'j'}, \omega_{ij}(x,y) \rangle, \\
K^{11}_{i'j'ij} &= \left\langle \ell_{i'j'}, (K\omega_{ij})\left(x,y,\frac{b}{a}\right)\right\rangle, \\
K^{12}_{i'j'ij} &= \left\langle \ell_{i'j'}, (K\omega_{ij})\left(y,x,\frac{a}{b}\right)\right\rangle, \\
K^{21}_{i'j'ij} &= \left\langle \ell_{i'j'}, (K\omega_{ij})\left(y,x,\frac{b}{a}\right)\right\rangle, \\
K^{22}_{i'j'ij} &= \left\langle \ell_{i'j'}, (K\omega_{ij})\left(x,y,\frac{a}{b}\right)\right\rangle, \\
F^{1}_{i'j'\alpha} &= \langle \ell_{i'j'}, f_\alpha(x,y) \rangle, \\
F^{2}_{i'j'\alpha} &= \langle \ell_{i'j'}, f_\alpha(y,x) \rangle,
\end{aligned} \tag{6}$$

where $\langle \ell, F \rangle$ represents the value of functional ℓ evaluated at function F (see appendix A2a).

Owing to the tight support properties of ω_{ij}, $\{E_{i'j'ij}\}$ is an upper-triangular sparse matrix. Whereas for $\left\{K^{\beta\gamma}_{i'j'ij}\right\}$ $(\beta = 1,2,\ \gamma = 1,2)$, the number of non-zero elements or equivalent two-dimensional singular integers to be calculated is $\sim 10^8$, which would cost considerable computation time. Fortunately, it was established that $\left\{K^{\beta\gamma}_{i'j'ij}\right\}$ can be approximated by a compressed sparse matrix $\left\{\widetilde{K^{\beta\gamma}_{i'j'ij}}\right\}$ [35]. A detailed compression algorithm is presented in appendix B. After constructing the coefficient matrix, $u^{\beta}_{ij\alpha}$ can be determined by solving equation (5). Subsequently, the screening current density can be obtained according to equation (4).

Finally, the MI, M_{cal}, is calculated by integrating the vector potential of the drive and screening currents around each loop of the pickup coil. In this study, we extracted the absolute λ by interpolating $M_{\mathrm{exp}}/M_{\mathrm{exp}}(T > T_{\mathrm{c}})$ into a lookup table consisting of $M_{\mathrm{cal}}/M_{\mathrm{cal}}(T > T_{\mathrm{c}})$ for different λ values.

4. Results and discussion

We characterized NbN#1 and NbN#2 using x-ray diffraction and our homemade *transmission*-type MI device. Figure 1(a) shows the x-ray diffraction $\theta - 2\theta$ scans for NbN#1 and NbN#2. Both films show a peak corresponding to the (200) peak of NbN, which crystallizes in the fcc structure. The raw MI data for NbN#1 is shown in figure 1(b). It is established that strong diamagnetic screening emerges when the sample enters the Meissner state at $T_{\mathrm{c}} \sim 14\,\mathrm{K}$, which is reflected as a sudden drop of V_x in the pickup coil (black line). Correspondingly, V_y shows a clear dip (red line), which may be attributed to energy dissipation mechanisms such as vortex-antivortex unbinding [18, 37]. In addition, the full width at half maximum of $V_y(T)$ is less than 1 K, indicating good film quality [3].

4.1. Breakdown of FLS method

We first employed the FLS method to extract λ (denoted as λ_{FLS}) of NbN#1 $\left(10 \times 10\,\mathrm{mm}^2\right)$ and NbN#2 $\left(5 \times 5\,\mathrm{mm}^2\right)$ from the MI, the details are described in [32]. Notably, the λ_{FLS} values of the two films exhibit significant discrepancies at low temperatures (figure 2). The $\lambda_{\mathrm{FLS}}\,(T = 4\,\mathrm{K})$ of NbN#2 is $\sim$10% higher than that of NbN#1. This phenomenon prompts us to recall the criterion given by Turneaure *et al* [24], which predicts that the FLS method fails when the film size is less than about five times the diameter of the coils. That is because the screening current reaches a significant peak at the film edge for small-sized films, which may cause a non-negligible contribution to M_1. Thus M_1 depends on λ, leading to the failure of the FLS method. Considering that the outer diameters of our coils are 1.3 mm, we speculate that the FLS method may be invalid for the NbN#2 with a size of $5 \times 5\,\mathrm{mm}^2$.

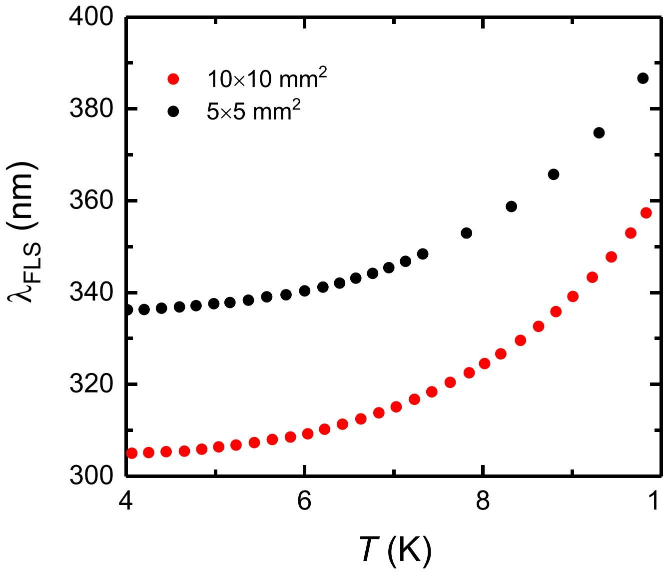

Figure 2. Temperature-dependent penetration depth, λ_{FLS}, of NbN#1 (red circles) and NbN#2 (black circles) extracted using the FLS method, showing non-negligible deviation at low temperature.

4.2. Calculated screening currents

To verify our speculation, we calculated the screening currents for square superconducting films with $d = 6.5\,\mathrm{nm}$ and $\lambda = 300\,\mathrm{nm}$ by solving equation (2). Figure 3 shows the normalized screening current densities, $j_{\mathrm{s}} = \sqrt{j^2_{\mathrm{sx}} + j^2_{\mathrm{sy}}}$, for the $5 \times 5\,\mathrm{mm}^2$ and $10 \times 10\,\mathrm{mm}^2$ films. They both attain a local maximum around the radius of the drive coil, which is consistent with previous reports [24, 25]. Notably, there indeed exists a significant peak at the edge of the $5 \times 5\,\mathrm{mm}^2$ film. In addition, the current density shows uneven distribution along film edge, which may come from the boundary condition without circular symmetry.

Thus, we conclude that the breakdown of the FLS method for small-sized films is due to the large screening current at the film edge, which is a crucial finding in this study. In addition, the breakdown will become more significant for smaller λ, when the screening current at the film edge is larger. As a result, the error of FLS method will increase with the decrease of temperature, as shown in figure 2.

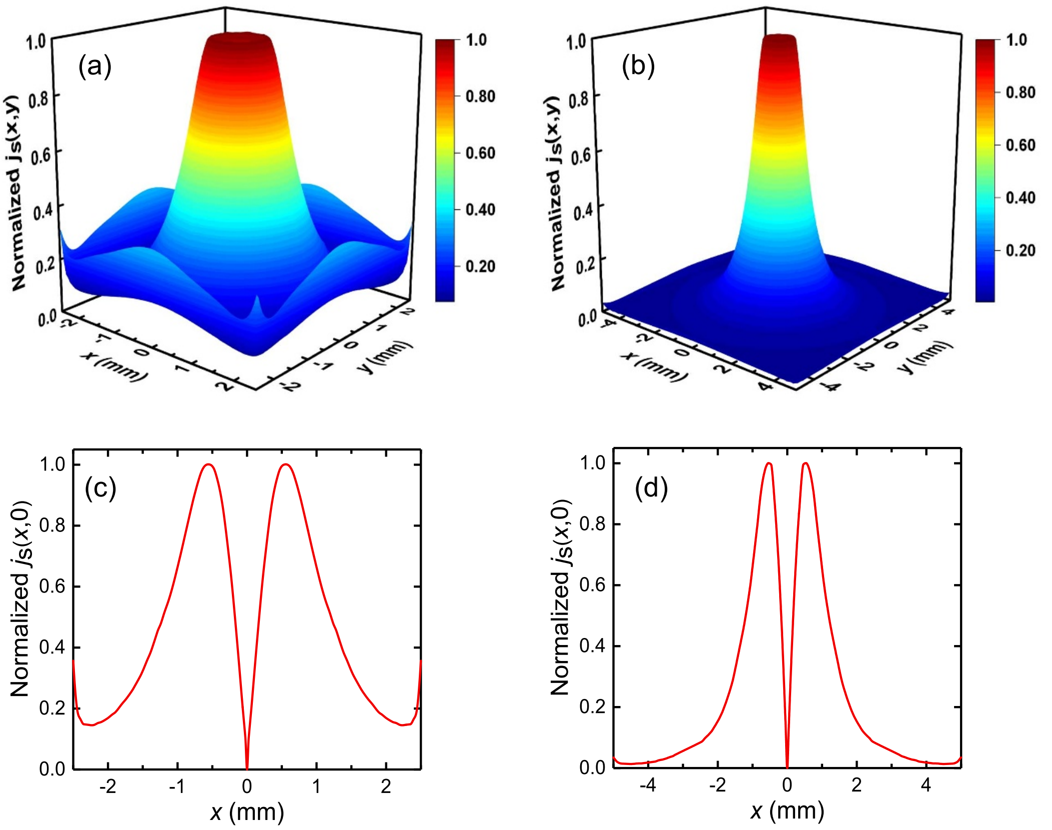

Figure 3. Normalized screening current densities $j_s = \sqrt{j_{sx}^2 + j_{sy}^2}$ for $5 \times 5\,\mathrm{mm}^2$ and $10 \times 10\,\mathrm{mm}^2$ superconducting films, calculated by the FWC method. (a), (b) Three-dimensional false-color plot of the normalized $j_s(x,y)$. (c), (d) Cuts of (a) and (b) at $y = 0$.

5. λ re-extracted using the FWC method

In contrast, the screening current at the film edge is considered in our numerical model, so the FWC method in principle works for small-sized films. To elucidate this, we re-extracted λ (denoted as λ_{FWC}) based on the lookup tables depicted in section 3. As shown in figure 4(a), the low-temperature data for the NbN#1 and NbN#2 are consistent. The difference in film size resulted in a deviation of only $\sim 1\,\mathrm{nm}$ in λ_{FWC} ($T = 4$ K). Moreover, the values of the extrapolated zero-temperature penetration depth $\lambda_{\mathrm{FWC}}(0)$ are consistent with the data in literature [19] (see figure 4(b)).

To summarize, we present the film-size-dependent λ extracted using the FLS and FWC methods in figure 4(c). It is established that for large-sized films (see the shadow region where the Turneaure criterion meets), λ_{FLS} is almost similar to λ_{FWC}. However, as the film size decreases, λ_{FLS} changes dramatically while λ_{FWC} remains almost unchanged. This indicates the applicability of the FWC method for small-sized superconducting films. In practice, when the film size is close to or less than the coil diameter, the position of the film with respect to the coils cannot be determined accurately, which may reduce the accuracy of the measurement of λ.

In addition, we tested the tolerance of the FWC method to different coil spacings. As shown in figure 4(d), the variation of λ_{FWC} is only 5% when the coil spacing reaches 1.6 mm. This spacing is sufficiently large for the ionic liquid gating experiment, which is a powerful tool for manipulating the superconducting properties continuously [38, 39].

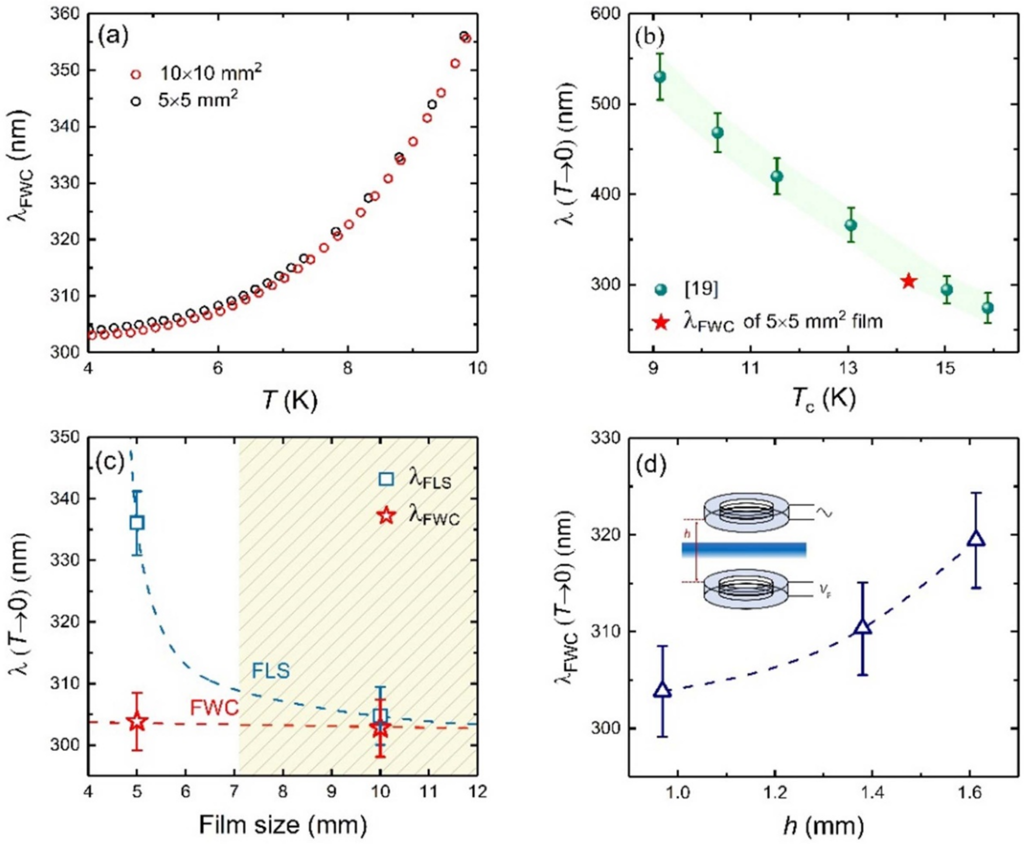

Figure 4. (a) Temperature-dependent λ_{FWC} of NbN#1 (red circles) and NbN#2 (black circles) extracted using the FWC method. (b) Value of λ_{FWC} $(T \to 0)$ for NbN#2 extracted using the FWC method, which shows a good agreement with the published data [19]; the length of error bar is shorter than the symbol size. (c) Film-size-dependent penetration depth extracted using the FLS and FWC methods. The shadow region indicates where the FLS method works [24]; the dashed line is a visual guide. (d) Measurements of λ_{FWC} $(T \to 0)$ for NbN#2 with different coil spacings.

6. Conclusions

In summary, we propose the FWC method for the MI technique to extract the absolute λ of polygonal superconducting films with arbitrary sizes. The experimental results on the square NbN films indicate that the absolute λ extracted using the FWC method is independent of the film size, whereas the conventional FLS method fails for the $5 \times 5\,\mathrm{mm}^2$ film because of the significant current peak at the film edge. This numerical method allows us to directly determine λ of small-sized superconducting films, dispensing with extra manipulations. In addition, for a coil spacing of 1.6 mm, the error in λ_{FWC} is only $\sim$5%. The high tolerance to coil spacing is promising in the *in situ* λ measurements integrated with ionic liquid gating technique, paving a high-efficiency way for the superconductivity research.

Data availability statement

All data that support the findings of this study are included within the article (and any supplementary files).

Acknowledgments

The authors would like to thank Liping Zhang and Zhanyi Zhao for performing the x-ray diffraction measurements. This work was supported by the Strategic Priority Research Program (B) of Chinese Academy of Sciences (XDB25000000), Key-Area Research and Development Program of Guangdong Province (2020B0101340002), the National Key Basic Research Program of China (2017YFA0302902, 2017YFA0303003 and 2018YFB0704102), the National Natural Science Foundation of China (11927808, 11834016, 118115301, 119611410 and 11961141008), the Key Research Program of Frontier Sciences, CAS (QYZDB-SSW-SLH008 and QYZDY-SSW-SLH001), CAS Interdisciplinary Innovation Team, and Beijing Natural Science Foundation (Z190008).

Appendix A. The multi-scale bases and collocation functionals

1. Multi-scale wavelets

We select the two-dimensional linear multi-scale wavelets $\omega_{ij}(x,y)$ $\left((x,y) \in E = \left\{(x,y) \in \mathbb{R}^2 : 0 \leqslant x \leqslant y \leqslant 1\right\}\right)$ in [36] to expand the screening currents, where subscript i represents the level of ω_{ij} and j represents the serial number of ω_{ij} at the ith level. For convenience, let $\mathbb{Z}_n = \{0, 1, \cdots, n-1\}$, and $\mathbb{Z}_n^m = \mathbb{Z}_n \times \mathbb{Z}_n \times \cdots \times \mathbb{Z}_n$. We further introduce a family of contract mappings $\Phi = \{\phi_i : i \in \mathbb{Z}_4\}$, which subdivide the unit triangle E into four triangles: $S_i = \phi_i(E)\ (i \in \mathbb{Z}_4)$. Note that different E corresponds to different ϕ_i functions. In our case, $\phi_0 = \left(\frac{x}{2}, \frac{y}{2}\right), \phi_1 = \left(\frac{x}{2}, \frac{y+1}{2}\right), \phi_2 = \left(\frac{1-x}{2}, 1-\frac{y}{2}\right), \phi_3 = \left(\frac{x+1}{2}, \frac{y+1}{2}\right)$.

The three wavelets at level 0 are constructed as

$$\begin{aligned} \omega_{00}(x,y) &= -3x + 2y, \\ \omega_{01}(x,y) &= 2 + x - 3y, \\ \omega_{02}(x,y) &= -1 + 2x + y. \end{aligned} \tag{A1a}$$

The nine wavelets at level 1 are given by

$$\begin{aligned}
\omega_{10}(x,y) &= \begin{cases} -\frac{11}{8} - \frac{15}{8}x + \frac{41}{8}y & (x,y) \in S_0, \\ \frac{5}{8} + \frac{1}{8}x - \frac{7}{8}y & (x,y) \in E \backslash S_0, \end{cases} \\
\omega_{11}(x,y) &= \begin{cases} 1 - \frac{15}{4}x - \frac{7}{8}y & (x,y) \in S_0, \\ -1 + \frac{1}{4}x + \frac{9}{8}y & (x,y) \in E \backslash S_0, \end{cases} \\
\omega_{12}(x,y) &= \begin{cases} \frac{9}{8} + \frac{15}{8}x - \frac{29}{8}y & (x,y) \in S_0, \\ -\frac{15}{8} - \frac{1}{8}x + \frac{19}{8}y & (x,y) \in E \backslash S_0, \end{cases} \\
\omega_{13}(x,y) &= \begin{cases} -\frac{15}{8} - \frac{41}{8}x + \frac{13}{4}y & (x,y) \in S_1, \\ \frac{1}{8} + \frac{7}{8}x - \frac{3}{4}y & (x,y) \in E \backslash S_1, \end{cases} \\
\omega_{14}(x,y) &= \begin{cases} \frac{29}{8} + \frac{7}{8}x - \frac{37}{8}y & (x,y) \in S_1, \\ -\frac{3}{8} - \frac{9}{8}x + \frac{11}{8}y & (x,y) \in E \backslash S_1, \end{cases} \\
\omega_{15}(x,y) &= \begin{cases} -\frac{5}{8} - \frac{29}{8}x + \frac{7}{4}y & (x,y) \in S_1, \\ \frac{3}{8} + \frac{19}{8}x - \frac{9}{4}y & (x,y) \in E \backslash S_1, \end{cases} \\
\omega_{16}(x,y) &= \begin{cases} \frac{15}{4} - \frac{13}{4}x - \frac{15}{8}y & (x,y) \in S_3, \\ -\frac{1}{4} + \frac{3}{4}x + \frac{1}{8}y & (x,y) \in E \backslash S_3, \end{cases} \\
\omega_{17}(x,y) &= \begin{cases} -\frac{1}{8} - \frac{37}{8}x + \frac{15}{4}y & (x,y) \in S_3, \\ -\frac{1}{8} + \frac{11}{8}x - \frac{1}{4}y & (x,y) \in E \backslash S_3, \end{cases} \\
\omega_{18}(x,y) &= \begin{cases} -\frac{5}{2} + \frac{7}{4}x + \frac{15}{8}y & (x,y) \in S_3, \\ \frac{1}{2} - \frac{9}{4}x - \frac{1}{8}y & (x,y) \in E \backslash S_3, \end{cases}
\end{aligned} \tag{A1b}$$

where $E \backslash S_i$ represents the set difference of S_i from E.

To generate high level wavelets ω_{ij} for $i \geqslant 2$, we introduce the composite map $\phi_{\mathbf{e}} = \phi_{e_0} \cdots \phi_{e_{n-1}}$, where $\mathbf{e} = (e_0, \cdots, e_{n-1}) \in \mathbb{Z}_4^n$ is an n-dimensional vector, and a number associated with $\mathbf{e}$ is defined as $\mu(\mathbf{e}) = \sum_{k=1}^{n} 4^{n-k} e_{k-1}$. Additionally, we define operators $\mathcal{T}_e\ (e \in \mathbb{Z}_4)$ by $\mathcal{T}_e F(x,y) = F\left(\phi_e^{-1}(x,y)\right) \chi_{S_e}(x,y)$, where χ_{S_e} denotes the characteristic function of set S_e. The corresponding composite operator is $\mathcal{T}_{\mathbf{e}} = \mathcal{T}_{e_0} \cdots \mathcal{T}_{e_{n-1}}$. Thereafter, the high-level multiscale wavelets, $\omega_{ij}\ (i \geqslant 2)$, are constructed as

$$\omega_{ij} = \mathcal{T}_{\mathbf{e}} \omega_{1l},\ j = 9\mu(\mathbf{e}) + l,\ e \in \mathbb{Z}_4^{i-1}, l \in \mathbb{Z}_9. \tag{A1c}$$

2. Collocation functionals

Using collocational functionals ℓ_{ij}, we can discretize equation (3) into equation (5), which is easier to handle. The concrete form of ℓ_{ij} is given in [36]. The three functionals of level 0 are given by

$$\ell_{0j} = \delta_{t_{0j}}, j \in \mathbb{Z}_4, \tag{A2a}$$

where $\delta_{t_{0j}}$ is the point evaluation functionals of three points $t_{00} = \left(\frac{1}{7}, \frac{5}{7}\right), t_{01} = \left(\frac{2}{7}, \frac{3}{7}\right), t_{02} = \left(\frac{4}{7}, \frac{6}{7}\right)$, and its effect on function F is defined as $\langle \delta_{t_{0j}}, F \rangle = F(t_{0j})$. The nine collocation functionals at level 1 are constructed as

$$\ell_{1l} = \sum_{e \in \mathbb{Z}_{12}} c_{le} \delta_{t_{1e}}, l \in \mathbb{Z}_9, \tag{A2b}$$

where $t_{1e} = \phi_i(t_{0j})\ (e = 3i + j,\ i \in \mathbb{Z}_4, j \in \mathbb{Z}_3)$ and the matrix $C = \{c_{le}\}_{9 \times 12}$ is constructed as

$$C = \begin{pmatrix} 0 & 1 & 0 & 0 & 1 & 0 & 0 & -1 & 0 & 0 & 0 & -1 \\ 0 & -1 & 0 & 0 & 1 & 1 & 0 & 0 & 0 & 0 & 0 & -1 \\ 0 & 1 & 0 & 0 & 0 & -1 & 0 & 0 & 1 & 0 & 0 & -1 \\ -1 & 0 & 0 & 1 & 0 & 0 & 0 & 0 & 1 & -1 & 0 & 0 \\ 1 & 0 & 0 & 0 & 0 & 0 & 0 & 0 & 1 & -1 & 0 & -1 \\ 1 & 0 & 0 & 0 & 0 & 1 & 0 & 0 & -1 & 0 & 0 & -1 \\ 0 & 0 & 1 & 0 & 0 & -1 & 1 & 0 & 0 & 0 & -1 & 0 \\ 0 & 0 & 1 & 0 & 0 & 1 & -1 & 0 & -1 & 0 & 0 & 0 \\ 0 & 0 & 1 & 0 & 0 & -1 & 0 & 0 & -1 & 0 & 0 & 1 \end{pmatrix}. \tag{A2c}$$

Subsequently, we introduce a linear operator, $\mathcal{L}_e$, defined for functional ℓ and function F by the equation, $\langle \mathcal{L}_e \ell, F \rangle = \langle \ell, F\phi_e \rangle$, and its composite operator $\mathcal{L}_{\mathbf{e}} = \mathcal{L}_{e_0} \cdots \mathcal{L}_{e_{n-1}}$. With the initial functionals, we can construct collocation functionals for $i \geqslant 2$ as

$$\ell_{ij} = \mathcal{L}_{\mathbf{e}} \ell_{1l}, j = 9\mu(\mathbf{e}) + l, e \in \mathbb{Z}_4^{i-1}, l \in \mathbb{Z}_9. \tag{A2d}$$

Appendix B. Block truncation scheme

Using block truncation schemes presented in [35], we can approximate matrix $\left\{K_{i'j'ij}^{\beta\gamma}\right\}$ $(\beta = 1, 2, \gamma = 1, 2)$ by a sparse matrix $\widetilde{\left\{K_{i'j'ij}^{\beta\gamma}\right\}}$. According to equation (6), the computation of matrix element $K_{i'j'ij}^{\beta\gamma}$ is associated with the corresponding $\ell_{i'j'}$ and ω_{ij}, which are further associated with a unique pair of vectors $\mathbf{e}'$ and $\mathbf{e}$ such that $\ell_{i'j'} = \mathcal{L}_{\mathbf{e}'} \ell_{1l'}$ and $\omega_{ij} = \mathcal{T}_{\mathbf{e}} \omega_{1l}$. Hence, $K_{i'j'ij}^{\beta\gamma}$ corresponds to a unique pair of $\mathbf{e}'$ and $\mathbf{e}$.

In addition, the contractive mapping $\phi_{\mathbf{e}}$ can map the unit triangle E into a smaller triangle $S_{ij}(E)$, which has a centroid(C_x, C_y). Therefore, we define $\Gamma(\mathbf{e}) = 4^{\frac{i-1}{2}}(C_x, C_y)$ and assign another pair of vectors $\mathbf{q}'$ and $\mathbf{q}$ to the matrix element $K_{i'j'ij}^{\beta\gamma}$ as follows:

(a) If $i \geqslant i\prime$, set $\mathbf{e_c} = (e_0, e_1, \cdots, e_{i'-2})$ and $\mathbf{q}' = \Gamma(\mathbf{e}')$, $\mathbf{q} = \Gamma(\mathbf{e_c})$.
(b) If $i < i\prime$, set $\mathbf{e}'_{\mathbf{c}} = \left(e'_0, e'_1, \cdots, e'_{i-2}\right)$ and $\mathbf{q}' = \Gamma(\mathbf{e}'_{\mathbf{c}})$, $\mathbf{q} = \Gamma(\mathbf{e})$.

Consequently, $\left\{K_{i'j'ij}^{\beta\gamma}\right\}$ can be divided into blocks $\left\{K_{\mathbf{q}'\mathbf{q}}^{\beta\gamma}\right\}$ according to $\mathbf{q}\prime$ and $\mathbf{q}$ as
$K_{\mathbf{q}'\mathbf{q}}^{\beta\gamma} = \left\{K_{i'j'ij}^{\beta\gamma} : K_{i'j'ij}^{\beta\gamma} \text{corresponds to the same pair } \mathbf{q}' \text{ and } \mathbf{q}\right\}$.

Given the truncation parameter $\sqrt{2} \leqslant r_{i'i} \leqslant \sqrt{3}$, the block truncation scheme indicates that $K^{\beta\gamma}_{\mathbf{q}'\mathbf{q}}$ can be replaced by

$$\widetilde{K^{\beta\gamma}_{\mathbf{q}'\mathbf{q}}} = \begin{cases} K^{\beta\gamma}_{\mathbf{q}'\mathbf{q}} & |\mathbf{q}-\mathbf{q}'| \leqslant r_{i'i}, \\ 0 & \text{otherwise.} \end{cases} \tag{B1}$$

ORCID iDs

Ruozhou Zhang https://orcid.org/0000-0002-4041-8570
Mingyang Qin https://orcid.org/0000-0001-5341-7465
Lixing You https://orcid.org/0000-0001-7304-0474
Peng Sha https://orcid.org/0000-0003-2545-7974
Qihong Chen https://orcid.org/0000-0002-6039-0456
Kui Jin https://orcid.org/0000-0003-2208-8501

References

[1] Tinkham M 1996 *Introduction to Superconductivity* (New York: McGraw-Hill)
[2] Hardy W N, Bonn D A, Morgan D C, Liang R and Zhang K 1993 *Phys. Rev. Lett.* **70** 3999–4002
[3] Skinta J A, Kim M S, Lemberger T R, Greibe T and Naito M 2002 *Phys. Rev. Lett.* **88** 207005
[4] Fletcher J D, Carrington A, Taylor O J, Kazakov S M and Karpinski J 2005 *Phys. Rev. Lett.* **95** 097005
[5] Uemura Y J *et al* 1989 *Phys. Rev. Lett.* **62** 2317–20
[6] Emery V J and Kivelson S A 1995 *Nature* **374** 434–7
[7] Hetel I, Lemberger T R and Randeria M 2007 *Nat. Phys.* **3** 700–2
[8] Broun D M, Huttema W A, Turner P J, Ozcan S, Morgan B, Liang R, Hardy W N and Bonn D A 2007 *Phys. Rev. Lett.* **99** 237003
[9] Franz M and Iyengar A P 2006 *Phys. Rev. Lett.* **96** 047007
[10] Hashimoto K *et al* 2012 *Science* **336** 1554
[11] Wang C G, Li Z, Yang J, Xing L Y, Dai G Y, Wang X C, Jin C Q, Zhou R and Zheng G Q 2018 *Phys. Rev. Lett.* **121** 167004
[12] Joshi K R, Nusran N M, Tanatar M A, Cho K, Bud'ko S L, Canfield P C, Fernandes R M, Levchenko A and Prozorov R 2020 *New J. Phys.* **22** 053037
[13] Gurevich A 2017 *Supercond. Sci. Technol.* **30** 034004
[14] Kubo T 2017 *Supercond. Sci. Technol.* **30** 023001
[15] Lin Z *et al* 2021 *Supercond. Sci. Technol.* **34** 015001
[16] Prozorov R and Giannetta R W 2006 *Supercond. Sci. Technol.* **19** R41–R67
[17] Prozorov R and Kogan V G 2011 *Rep. Prog. Phys.* **74** 124505
[18] Hebard A F and Fiory A T 1980 *Phys. Rev. Lett.* **44** 291–4
[19] Kamlapure A, Mondal M, Chand M, Mishra A, Jesudasan J, Bagwe V, Benfatto L, Tripathi V and Raychaudhuri P 2010 *Appl. Phys. Lett.* **96** 072509
[20] Bozovic I, He X, Wu J and Bollinger A T 2016 *Nature* **536** 309–11
[21] Yao G, Duan M C, Liu N, Wu Y, Guan D D, Wang S, Zheng H, Li Y Y, Liu C and Jia J F 2019 *Phys. Rev. Lett.* **123** 257001
[22] Claassen J H, Wilson M L, Byers J M and Adrian S 1997 *J. Appl. Phys.* **82** 3028–34
[23] Jeanneret B, Gavilano J L, Racine G A, Leemann C and Martinoli P 1989 *Appl. Phys. Lett.* **55** 2336–8
[24] Turneaure S J, Pesetski A A and Lemberger T R 1998 *J. Appl. Phys.* **83** 4334–43
[25] Turneaure S J, Ulm E R and Lemberger T R 1996 *J. Appl. Phys.* **79** 4221–7
[26] Duan M-C *et al* 2017 *Rev. Sci. Instrum.* **88** 073902
[27] Nam H, Su P H and Shih C K 2018 *Rev. Sci. Instrum.* **89** 043901
[28] Kinney J, Garcia-Barriocanal J and Goldman A M 2015 *Phys. Rev.* B **92** 100505
[29] Clem J R and Coffey M W 1992 *Phys. Rev.* B **46** 14662–74
[30] He X, Gozar A, Sundling R and Bozovic I 2016 *Rev. Sci. Instrum.* **87** 113903
[31] Fuchs A, Prusseit W, Berberich P and Kinder H 1996 *Phys. Rev.* B **53** R14745–R8
[32] Zhang R, Qin M, Zhang L, You L, Dong C, Sha P, Yuan J and Jin K 2020 *Acta Phys. Sin.* **69** 047401
[33] Zhang L *et al* 2018 *Sci. Rep.* **8** 1486
[34] Chen Z, Micchelli C A and Xu Y 2002 *SIAM J. Numer. Anal.* **40** 344–75
[35] Wang Y and Xu Y 2005 *J. Integr. Equat. Appl.* **17** 277–330
[36] Chen Z, Wu B and Xu Y 2008 *J. Integr. Equat. Appl.* **20** 49–92
[37] Leemann C, Lerch P, Racine G and Martinoli P 1986 *Phys. Rev. Lett.* **56** 1291–4
[38] Goldman A M 2014 *Annu. Rev. Mater. Res.* **44** 45–63
[39] Qin M *et al* 2020 *J. Supercond. Novel Magn.* **33** 159–63